



**HAL**  
open science

## Airport multipath simulation for siting DGPS reference stations

Christophe Macabiau, Benoit Roturier, Eric Chatre, Alain Renard

► **To cite this version:**

Christophe Macabiau, Benoit Roturier, Eric Chatre, Alain Renard. Airport multipath simulation for siting DGPS reference stations. ION NTM 1999, National Technical Meeting of The Institute of Navigation, Jan 1999, San Diego, United States. pp 135 - 144. hal-01021686

**HAL Id: hal-01021686**

**<https://enac.hal.science/hal-01021686>**

Submitted on 31 Oct 2014

**HAL** is a multi-disciplinary open access archive for the deposit and dissemination of scientific research documents, whether they are published or not. The documents may come from teaching and research institutions in France or abroad, or from public or private research centers.

L'archive ouverte pluridisciplinaire **HAL**, est destinée au dépôt et à la diffusion de documents scientifiques de niveau recherche, publiés ou non, émanant des établissements d'enseignement et de recherche français ou étrangers, des laboratoires publics ou privés.

# Airport Multipath Simulation for Siting DGPS Reference Stations

Christophe Macabiau and Benoît Roturier  
*CNS Research Laboratory of the ENAC*  
Eric Chatre *STNA*  
Alain Renard *SEXTANT AVIONIQUE*

Presented at ION NTM 99 on January 25th, 1999

## BIOGRAPHY

Christophe Macabiau is a Post-Doctoral researcher at the Ecole Nationale de l'Aviation Civile (ENAC) in Toulouse, France. After working in 1993 for the MLS Project Office in Ottawa, Canada, he received his Ph.D. from the Laboratoire de Traitement du Signal et des Télécommunications of the ENAC in 1997. He is currently working on the application of code and phase LADGPS positioning techniques to aeronautics.

Benoît Roturier graduated as an electronics engineer in 1985 from the Ecole Nationale de l'Aviation Civile (ENAC), Toulouse, France. After working for 18 months at Tahiti Faaa airport, French Polynesia, he led the Instrument Landing Team at the Service Technique de la Navigation Aérienne (STNA) in Paris from 1987 to 1989. Since 1990, he has been teaching and doing research at the ENAC, where he is currently in charge of the CNS Research Laboratory. He obtained his Ph.D. in 1995 from the Institut National Polytechnique de Toulouse (INPT). His current research area is propagation modeling for aeronautical telecommunication systems.

Eric Chatre graduated as an electronics engineer in 1992 from the ENAC (Ecole Nationale de l'Aviation Civile), Toulouse, France. Since 1994, he has been working with the Service Technique de la Navigation Aérienne (STNA) in Toulouse. He is involved in GNSS standardization activities in ICAO GNSSP and EUROCAE, RTCA forums.

Alain Renard is a GPS expert in the Advanced Studies division of the Navigation Department of SEXTANT AVIONIQUE. After graduating in 1972 as an engineer from the Ecole Nationale Supérieure d'Electronique et de Radioélectrique of Grenoble, he worked on radionavigation systems for commercial aircraft from 1973 to 1978. Then, he developed radionavigation systems based on OMEGA until 1988. Since 1988, he has been designing GPS and GLONASS navigation units.

## ABSTRACT

The siting of a GPS reference station on an airport is achieved by minimizing the influence of the environ-

ment on the pseudorange measurements, while complying with the practical operational installation constraints. The CNS Research Laboratory (URE-CNS) of the ENAC, in collaboration with the STNA and SEXTANT AVIONIQUE, has started a study that aims at providing siting guidelines for the French Civil Aviation Authority. As a result, a tool is developed, based on computed error predictions using mathematical models, and on signal disturbance measurements at preselected locations. The first part of this tool is an end-to-end GPS simulator that is used to establish the main basic rules for the choice of the best location of the station on an airport with regards to multipath effects. Its goal is to analyse the measurement errors induced by simple obstacles.

The aim of the proposed paper is to present the simulation software which was developed and some examples of the results it can provide.

The simulator is comprised of three cascaded modules. The first module computes the position of the satellites with a time step larger than the time of coherence of the propagation channel. The second module simulates the propagation channel. It is derived from the ray-tracing MUSICA tool (MULTipath SIMulation for Civil Aviation) that was previously developed by the ENAC for classical navaid's multipath simulation. Using the channel transfer function determined through the Uniform Theory of Diffraction, it generates the disturbed signal delivered by the antenna of the station to its receiver front-end. Then, this signal is handed to the last module, that simulates a generic GPS receiver and delivers the range measurement errors induced by the perturbations introduced in the whole propagation channel. The examples chosen show the ability to predict the influence of reflecting and diffracting objects, such as the ground and buildings on the code and phase measurement errors.

## I. INTRODUCTION

The pseudorange measurements made by a GPS receiver are disturbed by a combination of different errors such as satellite clock bias and SA, atmospheric propagation errors, tracking loop noise, and errors induced by the multipath propagation of the signal. The amplitude

and phase of the reflected and diffracted signals reaching the antenna depend on a high number of factors. Among them are the nature and size of the diffracting obstacles, the relative location and orientation of the receiving antenna with respect to these obstacles, the pattern and polarization of the antenna, and the processing operations performed within the receiver. Therefore, the multipath-induced errors affecting the measurements made by two distant receivers are different. As a consequence, the pseudorange corrections broadcast by a Local Area DGPS reference station can contaminate the measurements made by the user receiver with multipath errors that are proper to the reference station.

The multipath errors affecting the pseudorange corrections transmitted by the reference station can be reduced in several ways, including careful siting, good antenna design, and adequate signal processing. The study reported in this paper is focused on the selection of the siting location of the receiving antennas of an LADGPS reference station.

The perturbations caused by a complex airport environment on the pseudorange corrections transmitted by a Local Area DGPS reference station are difficult to determine because the transmitting satellites are in constant movement and because small obstacles can generate significantly disturbing signals. Therefore, it is necessary to elaborate a powerful tool to help the civil aviation authorities to select the best locations to install the reference stations. The functional principle of the siting tool can either be based on signal disturbance measurements at preselected locations or on computed error predictions based on mathematical models. Although both tools have major drawbacks, they are complementary.

Indeed, while the actual measurements correspond to real life situations, the variety of the field observations is restrained by physical constraints, and the assessment of all the safety critical situations is not possible in practice. On the other hand, the conformance of the simulations to reality is limited by the adequacy of the mathematical models, but initial results can be obtained faster for a very high number of representative situations, involving typical simple objects.

Therefore, the complete siting tool is built in two steps: first, a simulator is implemented, then a measuring instrument is developed, and both components are used in parallel to achieve our goal.

Several papers were published to report the work carried out on the prediction of environmental effects on GPS measurements, and the definition of obstacle clearance areas. [Gomez S. et al, 1995] and [Lippincott et al., 1996] have used the Uniform Theory of Diffraction to model GPS signal strength and phase shift generated by the obstacles, while [Walker R. et al, 1996] have used a parabolic equation technique. [Perez Fontan F. et al, 1998] applied their analysis to civil aviation, and

[Braasch M., 1992], [Weiser M., 1998] have focused on airport operation.

Our software combines propagation simulation and receiver simulation to provide straight predictions of measurement errors. The program, initially presented in [Maccabiau et al., 1998], treats multipath as a perturbation of the whole transfer function of the propagation channel. The signal is not modeled as a discrete sum of delayed and attenuated replicas, but as a transmitted signal modified by the transfer function of a global propagation channel. Therefore, our program takes into account most of the effects degrading the pseudorange measurements.

The validation of this simulation software is an important step. It is done in two stages. First, the results obtained from the simulations are compared with the theoretical results corresponding to the simulated situations, in order to check for flaws in the design and in the implementation of the algorithms. Next, measurement errors obtained in particular situations are compared to the errors predicted by the simulator for the same situations, as modeled by the users. The choice of the situations is critical, as they must be modeled as precisely as possible in order to be simulated with our software, and theoretical results must be available for these situations.

In this paper, we first describe the main points of the simulation software, such as its architecture and the underlying theoretical principles of the propagation and receiver modules. Next, we make a short introduction of the examples presented in this paper. Then, we show some examples of the results obtained using the software in different situations, like reflection from a ground plate, and diffractions from complex obstacles like building walls and edges. Finally, a conclusion is drawn from this study.

## II. PRESENTATION OF SIMULATION SOFTWARE

The end-to-end GPS simulator is software that simulates the effect of multipath on a GPS receiver. The input data is the position of the satellites at various epochs. The output data are the GPS observation errors, such as the pseudorange measurement errors.

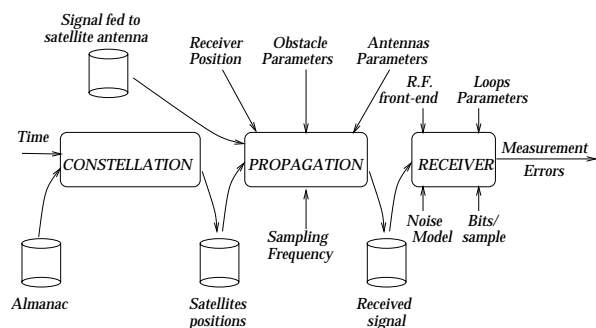


Figure 1: *Data flow in the simulator.*

The simulation is done using three processing modules written in MATLAB 5.2, that exchange data as illustrated in figure 1:

- The constellation module determines the positions of the GPS satellites in the WGS-84 reference frame using the input almanac file and the specified transmission time. The period used to sample the position of the satellites is equal to the sampling period of the transfer function of the propagation channel.
- The propagation module combines ray-tracing software based on the Uniform Theory of Diffraction adapted to GPS signals, and a signal generator that computes the baseband equivalent spectrum of the disturbed signal received from a particular satellite by the receiving antenna. The received signal is computed by filtering the signal fed to the transmitting antenna of the satellite by the calculated transfer function of the channel.
- The receiver module contains a model of a GPS receiver that simulates the operations performed by a receiver, in order to determine the measurement errors induced by multipath. The program computes the code and phase tracking errors by searching for the code and phase delay estimates that cancel the PLL and DLL control signals.

Specific models of the propagation channel and of the receiver processing operations were developed and inserted in the simulator.

The propagation channel is modeled as a linear time variant filter  $c$ , as presented in equation (1):

$$r(t) = \int_{-\infty}^{+\infty} e(t - \tau)c(\tau; t)d\tau \quad (1)$$

where

- $e$  is the signal fed to the transmitting antenna of the satellite. In our case,  $e$  is the power wave sent to the antenna.
- $r$  is the signal delivered by the receiving antenna. In our case,  $r$  is the power wave sent to the receiver front-end.
- $\tau$  is the argument of the weighting function  $c$  used to compute the filter output  $r$ .
- $t$  is the time at which the transfer function of the channel is applied.

In order to reduce the computation time, the propagation channel is sampled with a time interval larger than the internal sampling period of the receiver. As explained in [Macabiau et al., 1998], the transfer function is determined with a period lower than the time of coherence of the channel, which is of the order of a few seconds. At

each one of these sampling epochs, the characteristics of the channel are assumed to be constant, and a short slice of the received signal is generated.

Therefore, for each of the sampling epochs  $p$  of the transfer function of the channel, the received signal (1) can be expressed as:

$$r_p(n) = \sum_{m=-\infty}^{+\infty} e(n - m)c_p(m) \quad (2)$$

where

- $p$  represents the time at which the transfer function of the channel is sampled.
- $n$  describes the time evolution of the received signal.
- $m$  is the argument of the filter memory  $c$

The frequency domain equivalent of (2) is

$$R_p(k) = C_p(k)E(k) \quad (3)$$

The transfer function  $R_p(k)$  is determined by the propagation module for each frequency  $k\Delta f$  around L1. The Shannon theorem states that a signal must be sampled at a rate larger than twice the bandwidth of its Fourier transform. As recalled in [Macabiau et al., 1998], the bandwidth of the Fourier transform of the transfer function of the channel is the multipath delay spread of the channel. Therefore, the transfer function of the channel is sampled with a frequency step  $\Delta f$  lower or equal to half the coherence bandwidth  $\Delta f_c$  of the channel.

$$\Delta f < \frac{1}{2} \times \Delta f_c \quad (4)$$

The transfer function  $R_p(k)$  is determined by the ray-tracing software. The kernel of this software, called MUSICA (MULTipath SIMulation for Civil Aviation) was developed by the ENAC for classical nav aids [Roturier B., 1996]. This part of the software is based on the Uniform Theory of Diffraction (UTD).

The electromagnetic field radiated by the satellite antenna in any point of polar coordinates  $[r, \theta, \varphi]$  can be modeled as presented in equation (5).

$$\vec{E}(r, \theta, \varphi) = \sqrt{60P_T} \frac{e^{-ikr}}{r} G_{T_{max}} F_T(\theta, \varphi) \times \left( \frac{I_{Tx}}{|I_T|} \vec{\theta}_{Tx} + \frac{I_{Ty}}{|I_T|} \vec{\theta}_{Ty} + \frac{I_{Tz}}{|I_T|} \vec{\theta}_{Tz} \right) \quad (5)$$

where

- $P_T$  is the power of the signal fed to the antenna.
- $k = \frac{2\pi f}{c}$  is the wavenumber of the transmitted wave.
- $G_{T_{max}}$  is the maximum field gain of the transmitting antenna.

- $F_T$  is the normalized field radiation pattern of the transmitting antenna.
- $\vec{I}_T$  is the complex current vector of the transmitting antenna. Its complex components  $[I_{T_x}, I_{T_y}, I_{T_z}]$  are as depicted in figure 2.
- $\vec{\theta}_{T_x}, \vec{\theta}_{T_y}, \vec{\theta}_{T_z}$  are unit vectors defining the polarization of the radiated field, all orthogonal to the direction of propagation. For example, The vector  $\vec{\theta}_{T_x}$  is defined as  $\vec{\theta}_{T_x} = \frac{(\vec{U}_x \wedge \vec{r}) \wedge \vec{r}}{|\vec{I}_T \wedge \vec{r}|}$ , where  $\vec{U}_x$  is the vector defining the x axis.

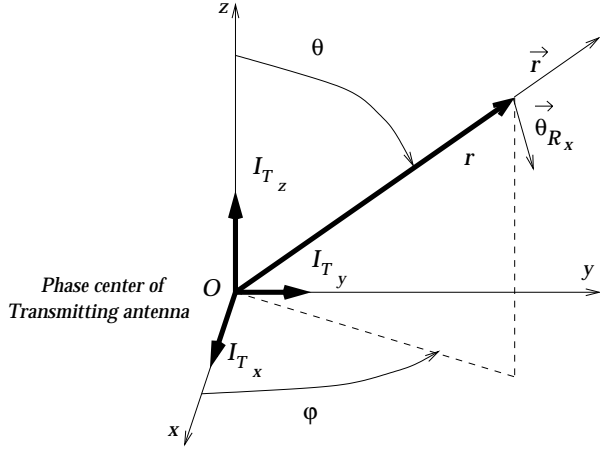


Figure 2: Polarization of the transmitted wave w.r.t the orientation of the transmitting antenna.

The computation of the electric field component is based on the ray theory. The electromagnetic ray is the portion of space that contributes significantly to the transport of the electromagnetic energy. This volume can be assimilated to the first Fresnel zone.

There are 5 types of rays, sorted by decreasing power: the direct ray, the reflected rays, the knife-edge diffracted rays, the corner diffracted rays and the creeping rays.

The rays that reach the receiver can have followed a complex path, resulting from several successive interactions with obstacles.

The interaction between the electromagnetic wave and an object is computed in two steps: first the rays are traced, then the reflexion and diffraction coefficients are computed.

The complex power wave  $R_i$  delivered by the incident ray  $i$  is modeled as in equation (6):

$$R_i(f) = \frac{1}{k\sqrt{120}} G_{R_{max}} F_R(\theta, \varphi) \times \left( \frac{I_{R_x}}{|I_R|} \vec{\theta}_{R_{x_i}} \cdot \vec{E}_i + \frac{I_{R_y}}{|I_R|} \vec{\theta}_{R_{y_i}} \cdot \vec{E}_i + \frac{I_{R_z}}{|I_R|} \vec{\theta}_{R_{z_i}} \cdot \vec{E}_i \right) \quad (6)$$

where

- $G_{R_{max}}$  is the maximum field gain of the receiving antenna.

- $F_R$  is the normalized field radiation pattern of the receiving antenna.
- $\vec{I}_R$  is the complex current vector of the receiving antenna. Its complex components  $[I_{R_x}, I_{R_y}, I_{R_z}]$  are as depicted in figure 3.
- $\vec{\theta}_{R_x}, \vec{\theta}_{R_y}, \vec{\theta}_{R_z}$  are unit vectors defining the polarization of the incoming field, all orthogonal to the direction of propagation. For example, the vector  $\vec{\theta}_{R_x}$  is defined as  $\vec{\theta}_{R_x} = \frac{(\vec{U}_x \wedge \vec{r}) \wedge \vec{r}}{|\vec{I}_R \wedge \vec{r}|}$ , where  $\vec{U}_x$  is the vector defining the x axis.

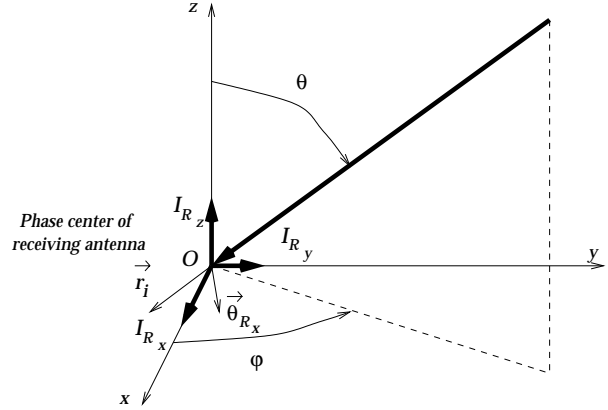


Figure 3: Polarization of the received wave w.r.t the orientation of the receiving antenna.

The transmitted power  $P_T$ , and the maximum field gains  $G_{T_{max}}$  and  $G_{R_{max}}$  are constant throughout the simulation. For each ray  $i$ , for each position of the satellites, and for each evaluation frequency  $k\Delta f$ , MUSICA uses  $F_T$ ,  $F_R$ ,  $\vec{I}_T$ , and  $\vec{I}_R$ , to compute the incident field  $\vec{E}_i$ , as well as the resulting power wave  $R_i(k\Delta f)$  delivered by the antenna. The total power wave delivered by the antenna is  $R(k\Delta f) = \sum_{i=0}^{N(t)} R_i(k\Delta f)$ . The transfer function of the propagation channel is then defined as:

$$C_p(k) = \frac{\sum_{i=0}^{N(t)} R_i(k)}{\sqrt{2P_T}} \quad (7)$$

The signal entering the receiver front-end is the result of the filtering of the input signal  $e$  by the propagation channel  $c$ .

The signal fed to the satellite antenna is modeled as:

$$e(t) = \sqrt{2P_T} C(t) D(t) \cos(2\pi f_0 t - \theta_0) \quad (8)$$

where

- $C$  is the C/A code of the transmitting satellite.
- $D$  is the navigation message.
- $f_0$  is the nominal L1 frequency.
- $\theta_0$  is an initial random phase.

This signal is a narrow band signal that can be modeled using the equivalent low pass signal  $e_{LP}$  such as

$$e(t) = \Re \{ e_{LP}(t) e^{i2\pi f_0 t} \} \quad (9)$$

where  $\Re \{ \}$  is the real part operator.

We can see that the equivalent low pass signal is necessarily complex:

$$e_{LP}(t) = \sqrt{2P_T} C(t) D(t) e^{-i\theta_0} \quad (10)$$

Similarly, the received signal  $r(t)$  is also a narrow band signal. Therefore, we can define  $r_{LP}(t)$  such that

$$r(t) = \Re \{ r_{LP}(t) e^{i2\pi f_0 t} \} \quad (11)$$

The operations performed within the RF front end are modeled as ideal amplification, frequency transposition, sampling and quantization, as depicted in figure 4.

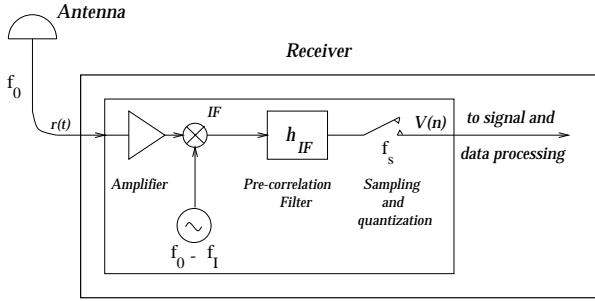


Figure 4: Model of the RF front-end used in the receiver simulator.

The digital signal delivered by the RF front-end is then modeled as

$$V(n) = Q \{ \Re \{ V_{LP}(nT_s) e^{i2\pi f_I nT_s} \} \} \quad (12)$$

where

- $Q \{ \}$  is the quantization operator.
- $V_{LP}$  is the equivalent low-pass signal resulting from the amplification and the filtering of  $r_{LP}$  by the RF front-end pre-correlation filter  $h_{IF}$ . We can write  $V_{LP}(t) = (h_{IF}(t) e^{-i2\pi f_I t}) \star e_{LP}(t)$ .
- $T_s$  is the sampling period.
- $f_I$  is the intermediate frequency.

Using these models, we can see that the equivalent low pass signal  $V_{LP}$  is such that

$$V_{LP}(t) = ((h_{IF}(u) e^{-i2\pi f_I u}) \star (c(u) e^{-i2\pi f_0 u}) \star e_{LP})(t) \quad (13)$$

The digital signal  $V(n)$  enters all the tracking channels of the receiver. In the following, we analyze the processing operations of one single tracking channel.

The receiver model used for this study is presented in figure 5.

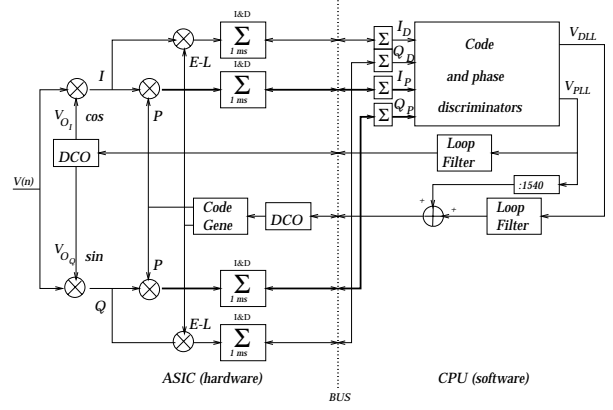


Figure 5: Main architecture of a GPS receiver tracking channel. Courtesy of SEXTANT AVIONIQUE [Renard A., 1997].

This input signal is converted into the I and Q channels, by mixing this signal with the DCO outputs  $V_{O_I}$  and  $V_{O_Q}$  such that

$$\begin{cases} V_{O_I}(n) = \cos \left( 2\pi f_I n T_s - \hat{\theta}(n) \right) \\ V_{O_Q}(n) = \sin \left( 2\pi f_I n T_s - \hat{\theta}(n) \right) \end{cases} \quad (14)$$

where  $\hat{\theta}(n)$  is the estimate of the incoming carrier phase.

The samples used by the phase tracking loop discriminator are  $I_P(k)$  and  $Q_P(k)$  as presented in equation (15).

$$\begin{cases} I_P(k) = K_0 \times \sum_{n=0}^{20ms} [V(n) \times V_{O_I}(n) \times C(nT_s - \hat{\tau}(k))] \\ Q_P(k) = K_0 \times \sum_{n=0}^{20ms} [V(n) \times V_{O_Q}(n) \times C(nT_s - \hat{\tau}(k))] \end{cases} \quad (15)$$

where  $K_0$  is the gain of the I and Q mixers.

The signals used by the code tracking loop are  $I_{D_{E-L}}(k)$  and  $Q_{D_{E-L}}(k)$ .

$$\begin{cases} I_{D_{E-L}}(k) = K_0 \times \sum_{n=0}^{20ms} [V(n) V_{O_I}(n) \times (C(nT_s - \hat{\tau}(k) - \frac{\Delta}{2}) - C(nT_s - \hat{\tau}(k) + \frac{\Delta}{2}))] \\ Q_{D_{E-L}}(k) = K_0 \times \sum_{n=0}^{20ms} [V(n) V_{O_Q}(n) \times (C(nT_s - \hat{\tau}(k) - \frac{\Delta}{2}) - C(nT_s - \hat{\tau}(k) + \frac{\Delta}{2}))] \end{cases} \quad (16)$$

where  $\hat{\tau}(n)$  is the code delay estimate and  $\Delta$  is the Early minus Late chip spacing.

Using the low-pass equivalent model presented in (12), the expression of the I and Q samples can be sim-

plified into:

$$\begin{cases} I_P(k) \approx \frac{K_0}{2} \sum_{n=0}^{20ms} \left[ Q \left\{ \Re \left\{ V_{LP}(n) e^{i\hat{\theta}(k)} \right\} \right\} \right] C(nT_s - \hat{\tau}(k)) \\ Q_P(k) \approx \frac{K_0}{2} \sum_{n=0}^{20ms} \left[ Q \left\{ \Re \left\{ iV_{LP}(n) e^{i\hat{\theta}(k)} \right\} \right\} \right] C(nT_s - \hat{\tau}(k)) \end{cases} \quad (17)$$

$$\begin{cases} I_{D_{E-L}}(k) \approx \frac{K_0}{2} \sum_{n=0}^{20ms} \left[ Q \left\{ \Re \left\{ V_{LP}(n) e^{i\hat{\theta}(k)} \right\} \right\} \right. \\ \quad \times \left. \left( C(nT_s - \hat{\tau}(k) - \frac{\Delta}{2}) - C(nT_s - \hat{\tau}(k) + \frac{\Delta}{2}) \right) \right] \\ Q_{D_{E-L}}(k) \approx \frac{K_0}{2} \sum_{n=0}^{20ms} \left[ Q \left\{ \Re \left\{ iV_{LP}(n) e^{i\hat{\theta}(k)} \right\} \right\} \right. \\ \quad \times \left. \left( C(nT_s - \hat{\tau}(k) - \frac{\Delta}{2}) - C(nT_s - \hat{\tau}(k) + \frac{\Delta}{2}) \right) \right] \end{cases} \quad (18)$$

The PLL and DLL control signals are computed using  $I_P(k)$ ,  $Q_P(k)$ ,  $I_{D_{E-L}}(k)$  and  $Q_{D_{E-L}}(k)$ . In the case of an arctangent PLL and a non-coherent dot-product DLL, for example, the PLL and DLL control signals are

$$\begin{cases} V_{PLL}(k) = \arctan \frac{Q_P(k)}{I_P(k)} \\ V_{DLL}(k) = \frac{I_{D_{E-L}}(k)I_P(k) + Q_{D_{E-L}}(k)Q_P(k)}{I_P^2(k) + Q_P^2(k)} \end{cases} \quad (19)$$

The PLL and the DLL are closed loop tracking devices that reach stable lock points in steady state if the signal to noise ratio is sufficient. These stable lock points are such that the discrimination function is canceled on a stable slope. Therefore, the determined tracking errors are the predicted values of  $\hat{\theta}(k)$  and  $\hat{\tau}(k)$  such that the PLL and DLL error signals reach a stable zero-crossing point, as indicated in (20).

$$\hat{\theta}(k) \text{ and } \hat{\tau}(k) \text{ are such that } \begin{cases} V_{PLL}(k) = 0 \\ V_{DLL}(k) = 0 \end{cases} \quad (20)$$

A few precautions have to be taken when computing the final tracking error using this technique:

- The tracking error due to noise can not be observed directly, instead its level has to be determined using classical equations.
- The signal to noise ratio has to be monitored to detect the situations where the loops lose track of the signal.
- When the error signals show several stable zero-crossing values, like for example when the direct and the reflected signal are separated by a time delay greater than the chip length plus half the Early-Late gate delay, the simulated result may not correspond to reality as the actual loops may lock on the reflected signal. This situation has to be flagged to the user.
- These predicted errors are raw tracking errors that don't take into account the other processing operations, such as code-phase smoothing for example. Further processing operations have to be reproduced on these predicted errors.

- This technique does not allow to simulate the transient tracking errors.

### III. PRESENTATION OF EXAMPLES

The software was tested in a number of classical configurations, and the output was checked against theoretical results. The examples presented in this paper are the output values at two stages of the simulator. This comprises the transfer function delivered by the propagation simulator, and the measurement errors provided by the receiver simulator. The output values are compared with the theoretical values as much as possible.

The transfer function is sampled every 5 seconds, with a frequency step  $\Delta f = 50$  kHz,  $\pm 3.5$  MHz around L1. Although all sorts of radiation patterns can be used by the simulator, in these examples, the simulated receiving antenna is an omnidirectional antenna. This is done to emphasize the influence of multipath, and to allow quick verification of the results.

The measurement errors delivered by the receiver simulator are the code and phase tracking errors. The simulated receiver is a narrow correlator receiver, with a chip spacing  $\Delta = 0.65T_c$ . The PLL is an arctangent costas loop, and the DLL is a non-coherent normalized dot-product tracking loop. The code and phase estimates are such that the DLL and PLL control signals are canceled.

The upper and lower bounds of the code tracking error  $\varepsilon_D(k)$  in the case of one single diffracted ray are plotted in figure 6 for a relative amplitude  $\alpha = 0.57$  and  $\alpha = 0.42$ , as these values are encountered in upcoming sections IV and V.

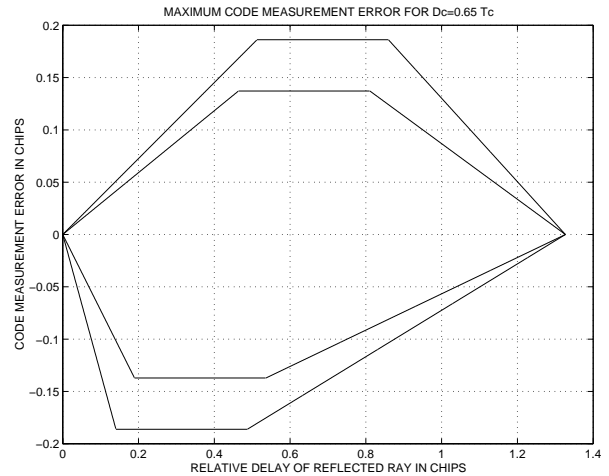


Figure 6: *Envelope of code measurement error for  $D_c = 0.65T_c$  and  $\alpha = 0.57$  and  $\alpha = 0.42$  (see sections IV and V).*

In the case of one single diffracted ray, the phase

tracking error can be approximated as:

$$\varepsilon_P(k) = \arctan \frac{\alpha \sin \Delta\varphi(k)}{1 + \alpha \sin \Delta\varphi(k)} \quad (21)$$

where

- $\alpha$  is the relative amplitude of both carriers entering the PLL after unspreading by the punctual code replica.
- $\Delta\varphi(k)$  is the relative phase shift between both carriers.

Two examples are presented in order to show the capability of the simulator.

In section IV, an omnidirectional antenna is simply placed above wet soil. The height of the antenna is changed from 50 m to 5 m. The results are shown for a high elevation satellite and for a low elevation satellite. The results obtained can be easily checked with classical results about one specular reflection.

In section V, the omnidirectional antenna is placed 5 m above the ground and close to a metallic building. The distance to the building is 10 m when tracking a high elevation satellite, and 100 m when tracking a low elevation satellite.

#### IV. ANTENNA ABOVE WET SOIL

Reflection off a ground plate gives place to a direct signal and a reflected signal.

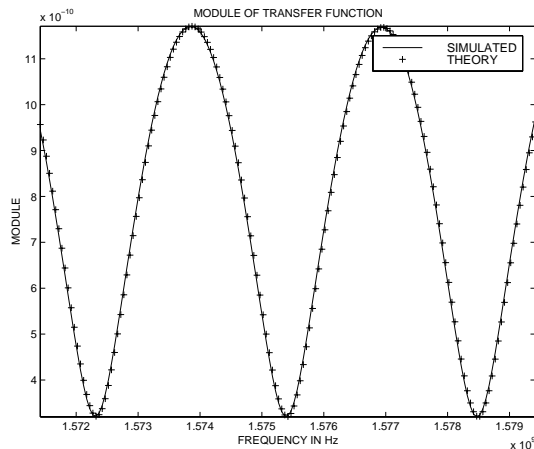


Figure 7: Module of the transfer function  $\pm 3.5$  MHz around  $L1$ .

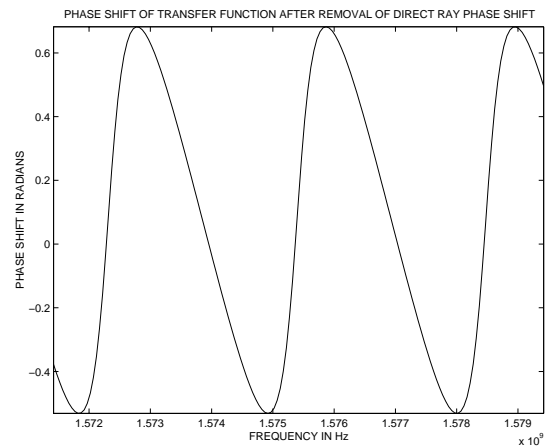
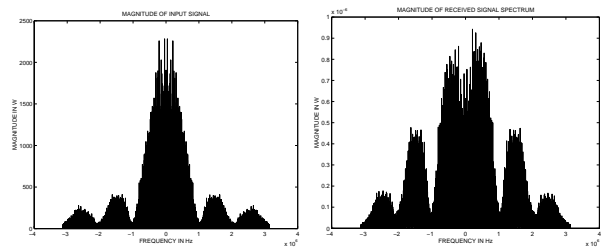


Figure 8: Phase of the transfer function  $\pm 3.5$  MHz around  $L1$ .

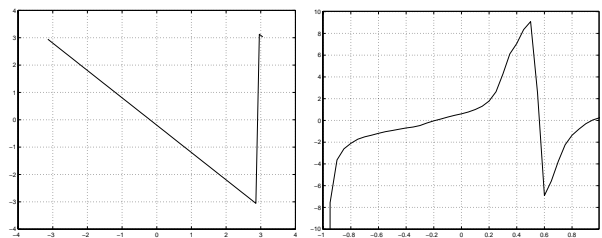
Figures 7 and 8 show the module and the phase shift of the transfer function at a particular epoch for an antenna located 50 m above a wet soil ground plate, and a satellite with an approximate elevation angle of 76 degrees. The magnitude of the soil reflection coefficient at  $L1$  for this elevation angle is approximately 0.57. These plots show the fading that will occur at some specific frequencies.

Figure 9(b) shows the deformation of the spectrum of the received signal at a particular epoch. This figure is to be compared with figure 9(a). It is visible that the central frequency components are severely affected by the transfer function plotted in figures 7 and 8.



(a) Spectrum of  $E(k)$ . (b) Spectrum of  $R(k)$ .

Figure 9: Comparison of spectrum of signal fed to satellite antenna  $E(k)$  and received signal  $R(k)$ .



(a) PLL ( $\varepsilon_P = -0.197$  rad.). (b) DLL ( $\varepsilon_D = -0.187T_c$ ).

Figure 10: PLL and DLL discriminators at a particular epoch.

Figures 10(a) and 10(b) show the PLL and DLL error signals  $V_{PLL}$  and  $V_{DLL}$  for the arctangent PLL discriminator and the dot-product DLL discriminator. As we can see, the stable lock points are not centered, as the multipath drives the loops away from the direct signal tracking. The PLL error signal cancels for  $\varepsilon_P = -0.197$  radians. The DLL error signal cancels with a tracking error  $\varepsilon_D = -0.187T_c$ .

Figures 11 and 12 show the code and phase tracking error in the situation depicted in figures 7 and 8, over a period of 5 minutes. The propagation channel is sampled with a 5 second period. The elevation angle of the satellite goes from  $76.5^\circ$  to  $74.3^\circ$ . The relative delay of the reflected ray goes from 97.2 m to 96.3 m, which is roughly  $0.33 T_c$ .

As we can see, the code tracking error shown in figure 11 is a periodic function. Its values are bounded by  $-0.18 T_c$  and  $0.12 T_c$ , or equivalently  $-53$  m and  $35$  m. These are the maximum values of the code tracking errors in this situation for this type of receiver, as indicated in figure 6. The phase tracking error shown in figure 12 is a periodic function as well, as expressed in (21). The total amplitude of the tracking error is compatible with (21), taking into account the additional attenuation of the reflected ray due to unspreading.

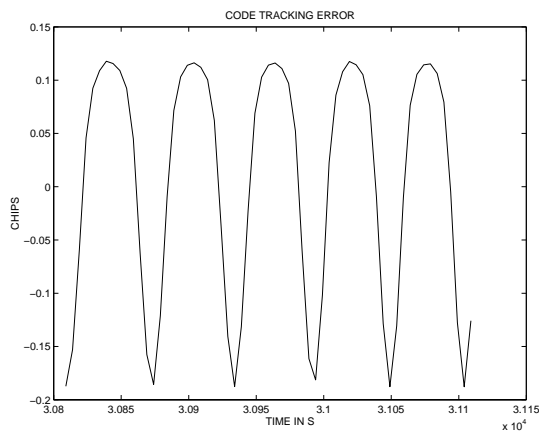


Figure 11: Code tracking error over 5 minutes for an omnidirectional antenna 50 m above wet soil.

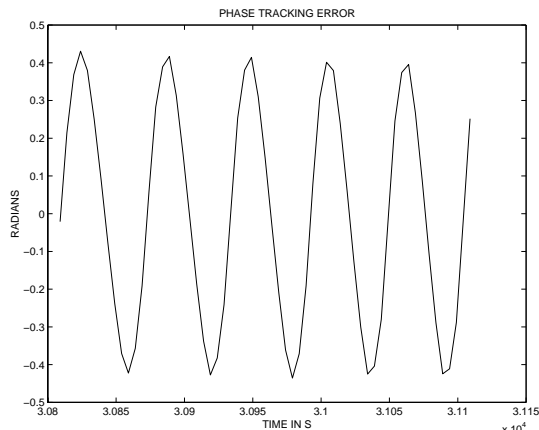


Figure 12: Phase tracking error over 5 minutes for an omnidirectional antenna 50 m above wet soil.

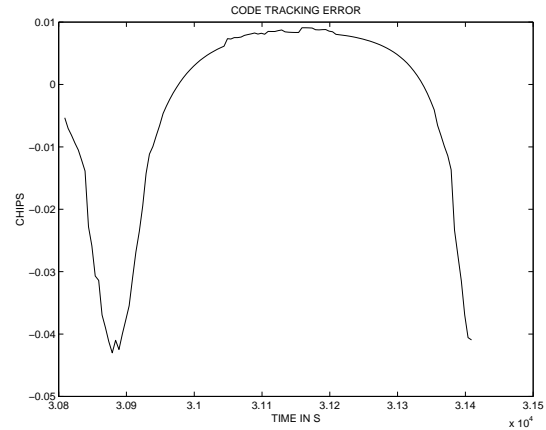


Figure 13: Code tracking error over 10 minutes for an omnidirectional antenna 5 m above wet soil.

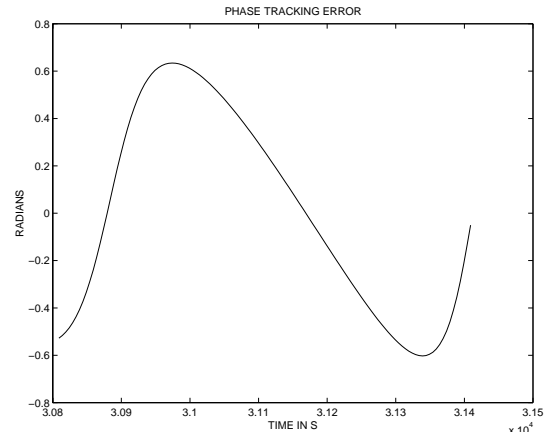


Figure 14: Phase tracking error over 10 minutes for an omnidirectional antenna 5 m above wet soil.

Figures 13 and 14 show the code and phase tracking errors in the case where the antenna is located 5 m above wet soil, for a period of 10 minutes in the same conditions. The relative delay of the reflected ray is now divided by 10, going from 9.7 m to 9.6 m, which is roughly  $0.03 T_c$ .

In that case, we can see that the period of the code and phase tracking error is much longer. In addition, the amplitude of the code tracking error is bounded with  $0.01 T_c$  and  $-0.042 T_c$ , or equivalently  $2.9$  m and  $-12.3$  m, which are the predicted values from figure 6. This is due to the fact that the relative delay of the reflected ray is shorter, therefore not perturbing much the DLL. The total amplitude of the phase tracking error, only driven by the relative attenuation of the incoming reflected carrier after unspreading is slightly increased. This is due to the fact that the reflected ray is less attenuated by the unspreading operation.

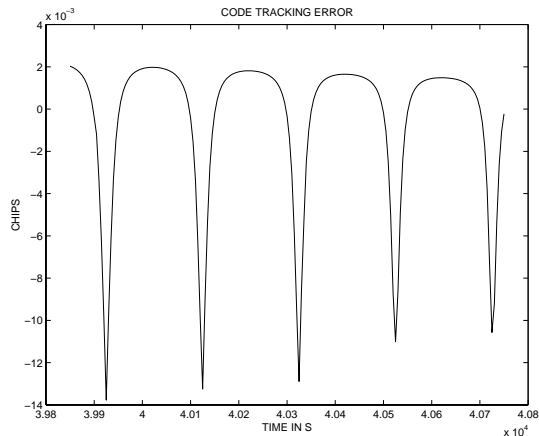


Figure 15: Code tracking error over 15 minutes for an omnidirectional antenna 5 m above wet soil.

Figure 15 shows the code tracking error in the case where the antenna is located 5 m above wet soil, for a period of 15 minutes, tracking the signal from a low elevation satellite. The elevation angle of the satellite goes from  $14.7^\circ$  to  $9.7^\circ$ . The amplitude of the wet soil reflection coefficient at this elevation angle is roughly 0.42. The relative delay of the reflected ray goes from 2.5 m to 1.7 m. The code tracking error is a periodic function, with a period larger than in the previous case due to the fast rotation of the phase as the satellite is going down. We can see that the amplitude of the code tracking error is much smaller, bounded by  $0.002 T_c$  and  $-0.014 T_c$ , or equivalently 0.6 m and -4.1 m. This is due to the fact that the relative delay of the reflected ray is shorter, therefore not perturbing much the DLL.

## V. ANTENNA CLOSE TO BUILDING

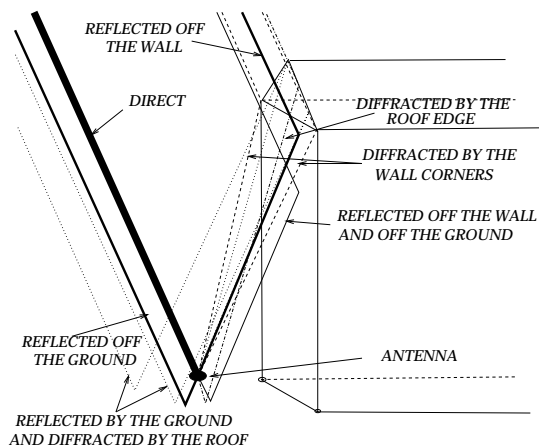


Figure 16: Ray-tracing for the antenna 5 m above wet soil, close to a metallic hangar.

In this example, the omnidirectional antenna is placed 5 m above wet soil, close to a metallic hangar. The antenna is hit by the direct ray, the ray reflected by the ground, and several reflected and diffracted rays coming from the hangar, as indicated in figure 16.

Figures 17 and 18 show the code and phase tracking error in the case where the antenna is located 10 m from the building, for a period of 10 minutes. The elevation angle of the satellite goes from  $78.6^\circ$  to  $74.3^\circ$ .

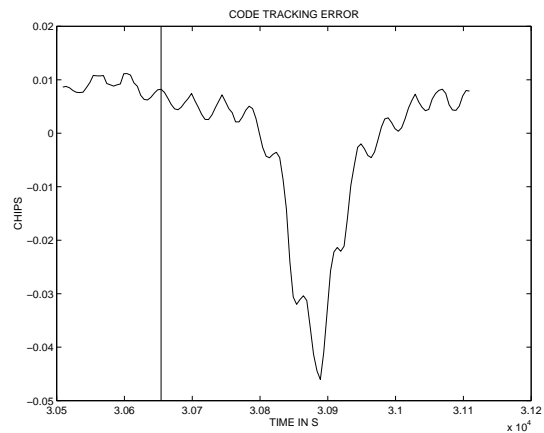


Figure 17: Code tracking error over 10 minutes for an omnidirectional antenna located 10 m away from a metallic building. The vertical line shows the time at which the wall reflects a ray that hits the antenna.

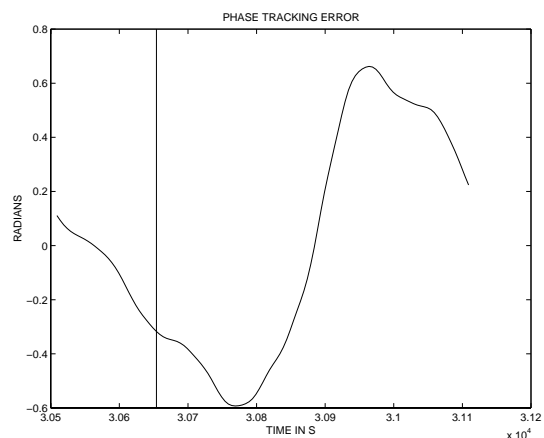


Figure 18: Phase tracking error over 10 minutes for an omnidirectional antenna located 10 m away from a metallic building. The vertical line shows the time at which the wall reflects a ray that hits the antenna.

As we can see, the evolution of the code tracking error has an overall appearance which is similar to the evolution plotted in figure 13. This indicates that the main disturbing ray is the ray reflected by the ground. However, small perturbations of the code tracking error can be seen on top of this mean value, which represent the contribution of the hangar to the tracking error. These small disturbances do not change when the ray reflected by the building wall hits the antenna, as indicated by the straight line in this figure. The perturbation due to the wall on the code tracking error is not significant, compared with the perturbation due to the ray reflected by the ground. This is due to the fact that the relative delays of the rays diffracted by the hangar are smaller than the relative delay of the ray reflected by the ground.

Figure 19 shows the code tracking error in the case where the antenna is located 100 m from the building, for a period of 15 minutes. The elevation angle of the satellite goes from  $14.7^\circ$  to  $9.7^\circ$ . We can see that the tracking error is not similar to the error plotted in figure 15. This is due to the fact that the main perturbing factor is the building, and not the ground in that case, as all the rays coming from the hangar have a large relative delay. The small oscillations are due to a ray diffracted by the building edges, and the influence of the ray reflected by the wall is very large, as the error increases up to  $0.3 T_c$  or 90 m after this ray hits the antenna, as indicated by the straight line.

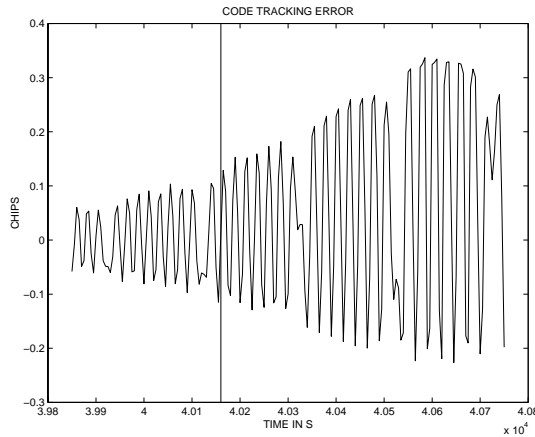


Figure 19: Code tracking error over 15 minutes for an omnidirectional antenna located 100 m away from a metallic building. The vertical line shows the time at which the wall reflects a ray that hits the antenna.

## VI. CONCLUSION

The software was checked against theoretical results in classical situations, and will undergo practical validation against real-life measurements during the next weeks.

The simulator can be used to analyze the impact of multipath in various configurations (obstacles, antenna, RF front-end, signal processing).

This simulator will be completed with a measuring tool to determine siting criteria in typical airport environments.

The simulator can also be used to characterize other effects in the transmission link (impact of satellite failure modes on receiver measurements for example).

## ACKNOWLEDGEMENTS

The authors wish to thank the company SEXTANT AVIONIQUE for providing advice and technical assistance, as well as the technical services branch of the french civil aviation authority, the STNA, for supporting this research.

## REFERENCES

- Braasch M. (1992)** "Characterization of GPS Multipath Errors in the Final Approach Environment", proceedings of ION GPS-92, The Institute of Navigation, Kansas City, Sept 16-18.
- Gomez S., Panneton R., Saunders P., Hwu S. and Lu B. (1995)** "GPS Multipath Modeling and Verification Using Geometrical Theory of Diffraction", proceedings of ION GPS-95, Palm Springs, September 12-15.
- Lippincott W., Milligan T. and Igli D. (1996)** "Method for Calculating Multipath Environment and Impact on GPS Receiver Solution Accuracy", proceedings of ION National Technical Meeting, Santa Monica, January 22-24.
- Macabiau C., Roturier B., Benhallam A., and Renard A. (1998)** "Development of an End-to-End GPS Simulator as a Tool for Siting GPS Reference Stations on Airport Platforms", proceedings of ION GPS-98, Nashville, September 15-18.
- Perez Fontan J., Vazquez Castro M. A., Kubista E., Paraboni A., Arbesser-Rastburg B., Buonomo S., and Poiaraes Baptista J. (1998)** "A Methodology for the Characterization of Environmental Effects on GNSS Propagation", International Journal of Satellite Communications, Vol 16, pages 1-22.
- Renard A. (1998)**, personal conversations with the authors.
- Roturier B. (1996)** "Modélisation de multitrajets par l'UTD pour les systèmes de radionavigation et communication de l'aviation civile", proceedings of JINA 1996, 12-14 November, pages 286-289.
- Walker R. and Kubik K. (1996)** "Numerical Modeling of GPS Signal Propagation", proceedings of ION GPS-96, Kansas City, September 17-20.
- Weiser M. (1998)** "Influence of GNSS Ground Station Siting on Multipath Errors", Working paper 16, ICAO GNSSP Working Group B meeting, Wellington, 23 February - 6 March.